Preprints (www.preprints.org) | NOT PEER-REVIEWED | Posted: 31 July 2019 doi:10.20944/preprints201907.0357.v1

Peer-reviewed version available at *Sensors* **2019**, *19*, 3954; doi:10.3390/s19183954

Article

Parametrically Amplified Low-Power MEMS Capacitive Humidity Sensor

Rugved Likhite [1], Aishwaryadev Banerjee [1], Apratim Majumder [1], Mohit Karkhanis [1], Hanseup Kim [1] and Carlos H. Mastrangelo [1,*]

[1] Department of Electrical and Computer Engineering, University of Utah, Salt Lake City, UT 84112, USA; rugved.likhite@utah.edu (R.L.); aishwaryadev.banerjee@utah.edu (A.B.); apratim.majumder@utah.edu (A.M.); mohit.karkhanis@utah.edu (M.K.); hanseup@ece.utah.edu (H.K.)

* Correspondence: carlos.mastrangelo@utah.edu (C.H.M); Tel.: +1-603-714-5099

Abstract: We present the design, fabrication, and response of a polymer-based Laterally Amplified Chemo-Mechanical (LACM) humidity sensor based on mechanical leveraging and parametric amplification. The device consists of a sense cantilever asymmetrically patterned with a polymer and flanked by two stationary electrodes on the sides. When exposed to a humidity change, the polymer swells after absorbing the analyte and causes the central cantilever to bend laterally towards one side, causing a change in the measured capacitance. The device features an intrinsic gain due to parametric amplification resulting in an enhanced signal-to-noise ratio (SNR). 11-fold magnification in sensor response was observed via voltage biasing of the side electrodes without the use of conventional electronic amplifiers. The sensor showed a repeatable and recoverable capacitance change of 11% when exposed to a change in relative humidity from 25-85%. The dynamic characterization of the device also revealed a response time ~1s and demonstrated a competitive response with respect to a commercially available reference chip.

Keywords: humidity sensor; low-power sensors; MEMS; parametric amplification; spring softening.

---

1. Introduction

In recent decades, miniaturized humidity sensors have been realized using various transduction methods [1–7] for a wide range of applications such as improving indoor comfort in homes and automobiles, humidity monitoring in semiconductor processing facilities [8], food processing industries [9], medical facilities [10] and, Internet-of-Things (IoT) based frameworks [11]. The push for the need for low-power chemical sensors [12–14] has been quite strong due to the growing importance of IoT sensor nodes across the world.

The most commonly used humidity sensor for the applications mentioned above is the capacitive sensor, which is used in nearly 75% of the cases [3] as it consumes near-zero DC power. These devices measure the change in capacitance caused by variations in dielectric properties or thickness of a sensing layer sandwiched between two parallel plates [15,16] when exposed to humidity. Sensors based on measuring the deflection of a microcantilever coated with a sensing polymer have also been demonstrated [17,18]. These sensors show a linear behavior, are easy to batch fabricate and most importantly, consume nearly zero DC power. However, their Signal-to-Noise Ratio (SNR) is usually limited by electronic noise as their sense capacitance can be small in comparison to the surrounding parasitics due to their small size [19]. Amplifiers are typically used in conjunction with such sensors to obtain a stable output which further adds to the total noise of the system and limits the SNR.

The sensitivity of capacitive hygrometers can be significantly improved if these devices have an intrinsic gain, thus reducing the dependence on noisy electronic amplifiers. This can be achieved with mechanical leveraging and parametric amplification. An example of a mechanically leveraged structure is a microcantilever device coated on one side with a sensing layer. Highly sensitive

© 2019 by the author(s). Distributed under a Creative Commons CC BY license.

Preprints (www.preprints.org) | NOT PEER-REVIEWED | Posted: 31 July 2019 doi:10.20944/preprints201907.0357.v1

Peer-reviewed version available at Sensors 2019, 19, 3954; doi:10.3390/s19183954

microcantilever-based sensors have been reported previously for detecting gases [18,20,21], DNA hybridization [22,23], and toxic chemical warfare agents [24]. In these devices, the exposure of the sensing film to an analyte generates surface stress that induces bending of the free-standing cantilever either due to a reduction in interfacial surface energy or swelling of the sensing layer. High signal to noise ratio can be realized in such devices using parametric amplification while maintaining small transducer size and low power consumption by exploiting the voltage induced lateral instability in MEMS devices to magnify their displacement to capacitance sensitivity. This technique has been previously reported to improve the performance of a MEMS magnetometer [19], gyroscope [25], hair-flow sensor [26], and vapor sensors [27–29]. Unlike electronic amplification, parametric amplification has an inherent advantage of providing higher sensitivity in MEMS sensor systems as it amplifies the sensor signal, without adding any extra electronic noise to the circuit.

In this paper, we report the design, fabrication, and testing of a new type of low power, batch-fabricatable parametrically amplified microcantilever-based humidity sensor with improved sensitivity. This article expands on a proof of concept presented earlier [29]. Extensive characterization of the sensor response has been presented in this article, along with dynamic response testing and comparison to a commercially available sensor. Additionally, a relevant analysis of the sensor output and a mathematical model describing the sensor action is also presented along with a study on the sorption kinetics of the device.

2. Device structure and operation

A unit cell of the LACM sensor is shown in Figure 1a. The device consists of a suspended microcantilever beam (electrode 2) asymmetrically coated on top with a sensing polymer (polyimide) and flanked on the sides by two stationary electrodes (1 and 3). When the device is exposed to an analyte vapor, the polyimide absorbs the gas and swells. This exerts a bending moment, M%RH, on the structural beam causing it to deflect to one side (Figure 1b). Unlike conventional polymer-based microcantilever sensors which measure the out-of-plane deflection of the cantilever [30], the LACM sensor measures the in-plane deflection of the sensing cantilever by forming two parallel plate variable capacitors between the central finger and the adjacent electrodes as shown below. Our devices are appropriately designed to make the out-of-plane stiffness much higher than the in-plane spring constant. A planer design allows multiple unit cell structures to be ganged up in parallel to increase the total output signal from the sensor (Figure 1c) while maintaining compatibility with conventional CMOS processes suitable for low power, high sensitivity water vapor sensor for application in IoT frameworks.

Furthermore, parametric amplification of the output signal is achieved by applying a symmetric DC bias voltage to both the flanking electrodes (1 and 3) w.r.t the central suspended electrode (2) to improve the vapor-concentration to displacement sensitivity of the device (Figure 1d). In this work, the single side capacitance measurements for the device have been reported. Theoretically, the sensor performance can be further improved by measuring a differential capacitance between the two sides while also eliminating common mode parasitics.

Preprints (www.preprints.org) | NOT PEER-REVIEWED | Posted: 31 July 2019 doi:10.20944/preprints201907.0357.v1

Peer-reviewed version available at Sensors 2019, 19, 3954; doi:10.3390/s19183954

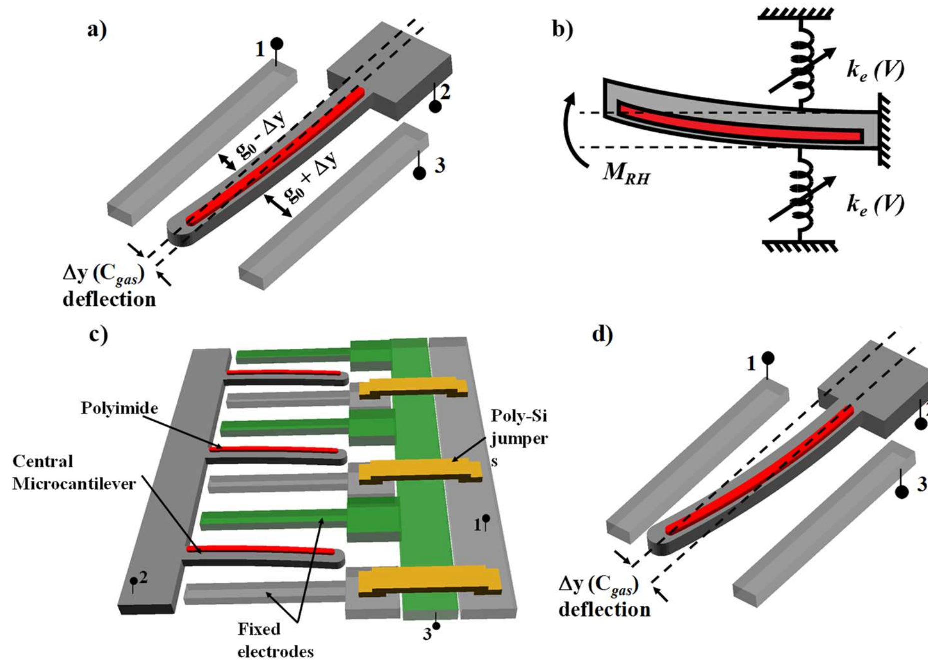

Figure 1: a) Unit cell of the LACM humidity sensor. b) Mechanical equivalent of the device when subjected to a change in relative humidity. c) Array structure of parallel LACM unit cells. d) Use of parametric amplification to magnify the deflection sensitivity of the central microcantilever.

85 *2.1. Electrostatic spring softening*

86 Parametric amplification induced spring softening in the mechanical domain has been
87 extensively studied to tune the resonant frequency of MEMS structures [31–33] and produce large-
88 amplitude deflections in microstructures [26,34]. In the LACM sensor, when a DC bias voltage is
89 applied to the electrodes 1 & 3 w.r.t electrode 2, the non-linearity of the electrostatic forces acting on
90 the central cantilever beams results in the reduction of the effective spring constant of the central
91 cantilever. Mathematically, electrostatic spring softening of micromechanical systems can be
92 observed by minimizing the total energy (U_T) function of the system,

93
$$U_T = U_{EL} + U_M \quad (1)$$

94 Where U_{EL} is the electrostatic energy stored in the capacitors of the system and U_M is the
95 mechanical energy stored in the deformed microcantilever beam. For a microcantilever beam
96 deflecting laterally between two electrodes, as shown in Figure 1, the respective energies can be
97 written as,

98
$$U_{EL} = \frac{-\varepsilon A V_b^2}{2}\left(\frac{1}{g_0+\Delta y} + \frac{1}{g_0-\Delta y}\right) \quad (2)$$

99
$$U_M = \frac{k_o \Delta y^2}{2} \quad (3)$$

100 Where, g_0 is the initial gap between the electrodes and Δy is the deflection of the central beam
101 due to absorption induced polymer swelling, V_b is the applied DC bias voltage, A is the overlap area
102 of the capacitor, ε is the permittivity and k_o is the lateral spring constant of the central finger when
103 no bias is applied. For $\frac{\Delta y}{g_0} \ll 1$, the total energy of the system can be written as,

104
$$U_T = \frac{1}{2}k_o\Delta y^2 - \left[\frac{\varepsilon A V_b^2}{g_0}\right]\left(\frac{1}{1-\left(\frac{\Delta y}{g_0}\right)^2}\right) \quad (4)$$

105
$$U_T = \frac{1}{2}k_o\left[\Delta y^2 - \left(\frac{2\varepsilon A V_b^2}{k_o g_0}\right)\left(1 + \left(\frac{\Delta y}{g_0}\right)^2 - \left(\frac{\Delta y}{g_0}\right)^4 + \ldots..\right)\right] \quad (5)$$

106
$$U_T \cong \underbrace{\frac{1}{2}k_o\left[1 - \left(\frac{2\varepsilon A V_b^2}{k_o g_0^3}\right)\right]}_{k(M)}\Delta y^2 + h.o.t \quad (6)$$

107

Preprints (www.preprints.org) | NOT PEER-REVIEWED | Posted: 31 July 2019 doi:10.20944/preprints201907.0357.v1

Peer-reviewed version available at Sensors 2019, 19, 3954; doi:10.3390/s19183954

For $V_p = \sqrt{\frac{k_o g_0^3}{2\varepsilon}}$, which is the differential pull-in voltage for the structure, the effective softened spring constant k(M), can be written as,

$$k(M) = \frac{k_o}{M} \; where, M = \frac{1}{\left(1-\frac{V_b^2}{V_p^2}\right)} \quad (7)$$

For example, Figure 2a shows the total energy of a system with k_o = 3.7 Nm^{-1} and V_p = 35.4V without DC bias (V_1 = 0V) and, when DC voltage bias (V_2 = 18V and V_3 = 28V) is applied to induce parametric amplification, as a function of normalized beam deflection. As the magnitude of the applied voltage bias is increased, the system becomes progressively unstable due to shallowing of the local energy minima. Since $k(M) < k_o$, the output signal is magnified by a voltage-dependent magnification factor, M, as shown in Figure 2b.

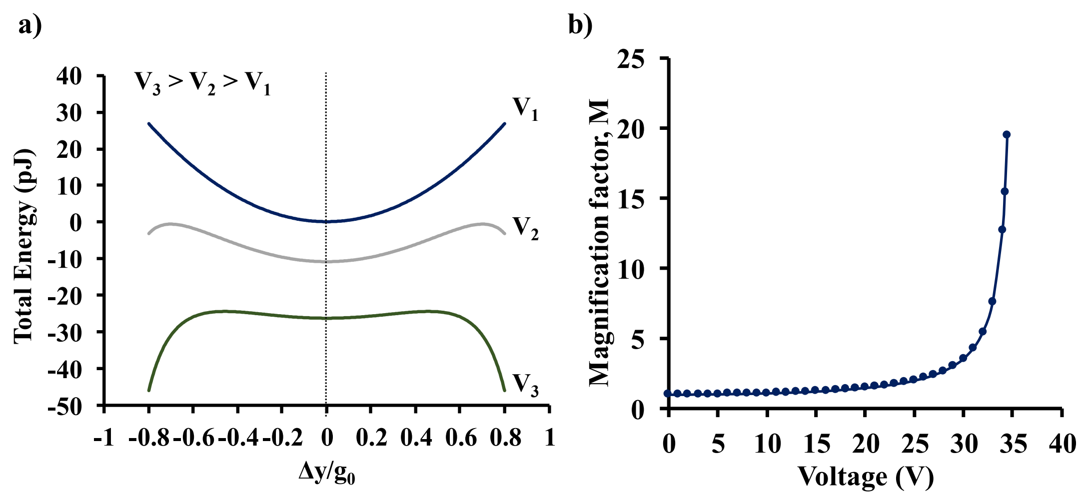

Figure 2: Schematic of the a) Total energy of the system during parametric amplification, b) Magnification factor, M as a function of the applied voltage.

2.2. Noise Analysis and Signal-to-Noise Ratio

The noise of the system originates from both the mechanical-thermal noise [35,36] of the deflecting beam and the noise of the C/V converter operational amplifiers [37]. In our device, we convert the stress caused by the RH absorption into a mechanical deflection which translates into a variable, RH dependent capacitance, mediated through the beam spring constant $k(M)= k_o/M$, where M is the bias-dependent magnification factor. We use high-gain op-amps to amplify and read the sensor capacitance [38] as illustrated in the schematic of Figure 3a below.

Preprints (www.preprints.org) | NOT PEER-REVIEWED | Posted: 31 July 2019 doi:10.20944/preprints201907.0357.v1

Peer-reviewed version available at Sensors 2019, 19, 3954; doi:10.3390/s19183954

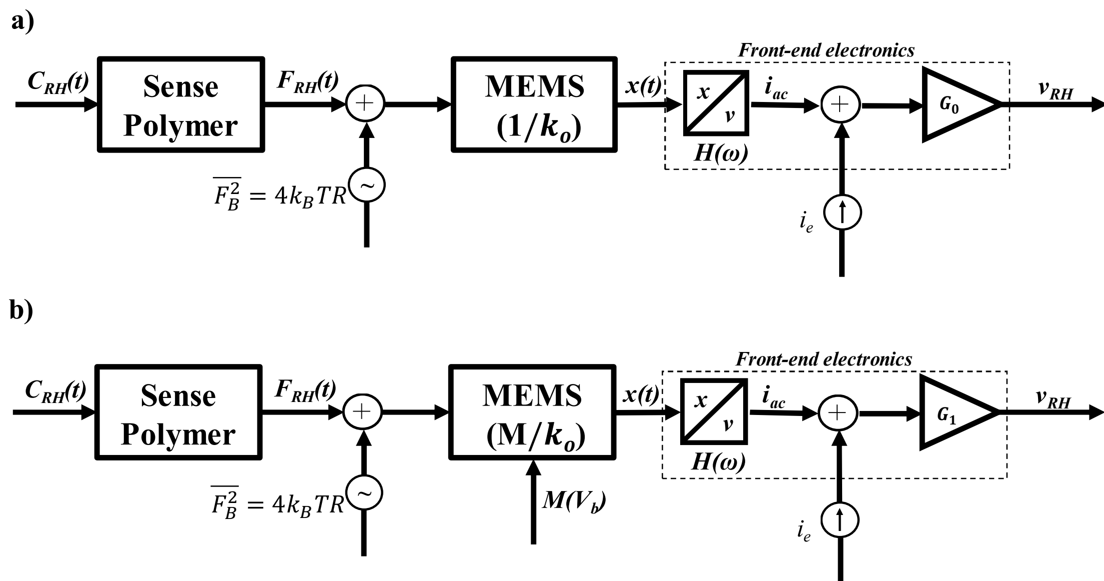

Figure 3: a) Schematic of the sensor system at zero bias with default spring constant k_o. b) With parametric amplification (near-Brownian noise limited)

124 The capacitance change indicative of the vapor concentration signal is first converted to an AC
125 current $i_{ac} = j\omega C(RH) \cdot V_o$, where V_o is the amplitude of a sinusoidal AC voltage of angular
126 frequency ω placed across the capacitor. The AC current is finally converted to an output voltage
127 using a high-gain op-amp of transconductance G_o. The noise of the system is calculated by the
128 introduction of two noise sources: (1) a mechanical noise acting on the beam with spectral density
129 [35,39],

130 $$F_B = \sqrt{4k_B TR} \qquad [N/\sqrt{Hz}] \tag{8}$$

131 Which, is only dependent on the Boltzmann constant k_B, temperature T, and, viscous damping
132 coefficient R, of the system, as described previously in a viscous damping environment (air) and, at
133 low pressures [36]. Therefore, the noise force on the MEMS device is completely independent of the
134 bias induced spring-softening used in the LACM sensor. (2) The electronic noise current source $\overline{i_e^2}$,
135 which is introduced at the input of the transconductance amplifier. The output noise for this system
136 is thus

137 $$\overline{v_o^2\ (k_o)} = G_o^2 \left(\omega^2 V_o^2\ F^2 \frac{\overline{F_B^2}}{k(M)^2} + \overline{i_e^2} \right)$$

138 $$= G_o^2 \left(\omega^2 V_o^2\ F^2 \frac{\overline{F_B^2}}{k_o^2} + \overline{i_e^2} \right) = G_o^2 \left(H^2(\omega) \cdot \frac{\overline{F_B^2}}{k_o^2} + \overline{i_e^2} \right) \tag{9}$$

139 Where,

140 $$H^2(\omega) = \omega^2 V_o^2\ F^2 \qquad , F^2 = \left(\frac{dC}{dF_B}\right)^2 \tag{10}$$

141 And since the deterministic signal $v_{RH}^2 = H^2(\omega) \cdot \frac{F_{RH}^2}{k_o^2} \cdot G_o^2$, where F_{RH} is the equivalent RH-
142 driven force, the signal to noise ratio is thus given by:

143 $$SNR_o = \frac{\frac{F_{RH}}{k_o} \cdot H(\omega)}{\sqrt{\frac{F_B^2}{k_o^2} \cdot H^2(\omega) + i_e^2}} = \frac{\left(\frac{F_{RH}}{F_B}\right)}{\sqrt{1 + \left(\frac{k_o^2}{H^2(\omega) \cdot F_B^2}\right) \cdot i_e^2}}$$

144 $$= \frac{SNR_{max}}{\sqrt{1 + \left(\frac{k_o^2}{H^2(\omega) \cdot F_B^2}\right) \cdot i_e^2}} \tag{11}$$

145

146 It is evident that the SNR is independent of transconductance G_o. Eq. (11) also tells us that any
147 electromechanical effect that lowers k_o will result in a higher SNR. In our device, this can be achieved
148 with the bias-induced spring softening gain M, as shown in the schematic of Figure 3b such that

Preprints (www.preprints.org) | NOT PEER-REVIEWED | Posted: 31 July 2019 doi:10.20944/preprints201907.0357.v1

Peer-reviewed version available at Sensors 2019, 19, 3954; doi:10.3390/s19183954

$$SNR(M) = \frac{SNR_{max}}{\sqrt{1 + \frac{\left(\left(\frac{SNR_{max}}{SNR_O}\right)^2 - 1\right)}{M^2}}} \tag{12}$$

The SNR is improved for M > 1 essentially because the spring softening effect gain is noiseless, thus moving the electronic noise closer to the amplified output.

2.3. Sensor response model

The LACM sensor is essentially a humidity-dependent variable parallel-plate capacitor. When the device is exposed to humidity, the sensing polymer swells after absorbing the water vapor. Since the polymer is asymmetrically patterned and constrained to the silicon cantilever beam, the swelling generates surface stress [40], which results in the bending of the cantilever beam towards one side. This results in a change in the measured capacitance of the device. The amount of cantilever bending and, therefore, the capacitance change is directly proportional to the swelled induced surface stress and inversely proportional to the effective spring constant of the device given by equation (7). This can be mathematically described by a modified form of Stoney's equation as given by Godin et al. [41].

For small displacements of the central cantilever beam, the normalized change in capacitance can be written as,

$$\frac{\Delta C}{C} = (A_o)\left[\frac{(1-\nu)l^2}{g_o E_{Si} w^2} \cdot \frac{1}{\left(1-\frac{V^2}{V_p^2}\right)} . \beta_p . C_{RH}\right] + B_o \tag{13}$$

Where, ν = Poisson's ratio of Silicon, l = length of central cantilever beam, g_0 = initial air-gap between electrodes, E_{Si} = Young's Modulus of Silicon, w = width of central cantilever beam, V = applied voltage bias to induce spring softening, V_p = differential pull-in voltage of beam, β_p = fitting parameter proportional to the swelling-induced surface stress generated by the polyimide and C_{RH} is the relative humidity of the chamber. A_o and B_o are dimensionless fitting parameters.

2.4. 2-level electrical interconnects

The laterally deflecting and planar design of the LACM sensor allows connecting multiple unit cells in parallel to further increase the output of the sensor. Since each microcantilever is flanked on the two sides by electrically isolated anchored electrodes, it is necessary to have a 2-level electrical connection arrangement in the device. In the LACM sensor array, this is done by fabricating jumpers out of doped poly-Si, as shown in Figure 1c. The detailed fabrication procedure is described in the following sections. The jumper arrangement eliminates the needs for wire bonds to connect multiple devices, thus keeping the fabrication process simple.

3. Fabrication and Imaging

3.1. Device Fabrication

Figure 4(a-l) shows a simplified fabrication procedure of the device. The process starts by depositing 250nm of low-stress silicon nitride using LPCVD process over SOI wafers with 30 µm thick device layer and 2 µm thick buried oxide layer, as shown in Figure 4a. The nitride layer is patterned using conventional UV photolithography with and then etched using CF_4/O_2 RIE. The device layer of the SOI wafer is then etched using DRIE to form the fingers (Figure 4b). A low-frequency RF source (380 kHz) is used for this process to avoid footing and prevent premature release of the device. The photoresist is then removed using Acetone, and a pre-furnace clean is performed. A 100nm thin layer of LPCVD silicon nitride is then deposited on the wafer, and a blanket CF_4/O_2 RIE etch is done. This ensures that the nitride remains only on the sidewalls of the etched fingers (Figure 4c). A 4µm thick layer of sacrificial LPCVD PSG is then deposited on the wafer and annealed in an N_2 environment at 1050°C to reflow the PSG. The thickness of the PSG is then reduced to ~2 µm using a blanket RIE etch on the wafer. This deposition-reflow and etch back process is repeated until the

Preprints (www.preprints.org) | NOT PEER-REVIEWED | Posted: 31 July 2019 doi:10.20944/preprints201907.0357.v1

Peer-reviewed version available at Sensors 2019, 19, 3954; doi:10.3390/s19183954

193 etched gaps between different fingers are entirely sealed (Figure 4d) due to the cusping effect in an
194 LPCVD process thus allowing further processing of the wafer [42,43]. The sacrificial PSG and the
195 underlying nitride are then patterned using photolithography and RIE to create anchors (Figure 4e)
196 for poly-Si jumpers and the anti-stiction micro-staple pins. A 4 µm thick layer of poly-Si is then
197 deposited using LPCVD process. This layer is then doped using phosphorus solid-source doping and
198 annealed at 1050°C for 2 hours (Figure 4f). A 200nm thick layer of Cr is then deposited over the wafer
199 using DC-sputtering and patterned using a wet etchant to form the metal contact and jumpers (Figure
200 4g). The wafer is the then cleaned, and the anti-stiction features are patterned (Figure 4h). This step
201 also forms the poly-Si jumpers and contact pads, with the previously patterned Cr metal acting as an
202 etch mask. The PSG on the central finger is then patterned and etched to create windows (Figure 4i)
203 to allow deposition and anchoring of the sensing polymer to the device. We use HD-4104 polyimide
204 [44] as a water vapor sensing material. The polyimide was spin-coated on the sample and then cured
205 in at 300°C in an N_2 environment for 3 hours. A commercially available Polyimide adhesion
206 promoter, VM-651, was applied to the sample before spin-coating to improve the adhesion of the
207 polyimide to the substrate and prevent any delamination during the BOE release procedure. A 200nm
208 thick Al layer is then sputtered on the polyimide and then patterned using wet etching to act as a
209 hard mask. The polyimide is then etched using O_2 plasma (Figure 4j) in an Oxford 100 ICP etcher.
210 The devices are then diced, and the chips are released in BOE for 160 mins with constant stirring
211 (Figure 4k). The chips are rinsed thoroughly in DI water followed by methanol and allowed to air
212 dry.

213 *3.2. Stiction Suppression*

214 Stiction is one of the main modes of failure in MEMS devices [45]. Device failure due to stiction
215 occurs when suspended MEMS structures such as cantilevers, plates, or beams adhere to the substrate
216 or adjacent features due to lack of sufficient restoring force when subjected to strong capillary forces.
217 Typically, capillary forces arise during device fabrication and cleaning due to the surface tension of
218 water when the sample is allowed to dry. Various methods have been previously used to prevent
219 stiction due to surface tension [45–47]. In the LACM device, a different method which utilizes 'micro
220 staple-pins,' that hold the released cantilever in place during a wet release procedure has been
221 utilized. The staples are made out of thin poly-Si which can be dry etched, thus eliminating the need
222 for complex and expensive anti-stiction processes.
223 A very short SF_6 etch is finally performed on the devices to etch away the anti-stiction micro-
224 staples and release the fingers (Figure 4l). Any unwanted etching on the side wall of the fingers is
225 prevented by the thin Si_3N_4 film that was deposited over the finger before PSG sealing.

Preprints (www.preprints.org) | NOT PEER-REVIEWED | Posted: 31 July 2019 doi:10.20944/preprints201907.0357.v1

Peer-reviewed version available at Sensors 2019, 19, 3954; doi:10.3390/s19183954

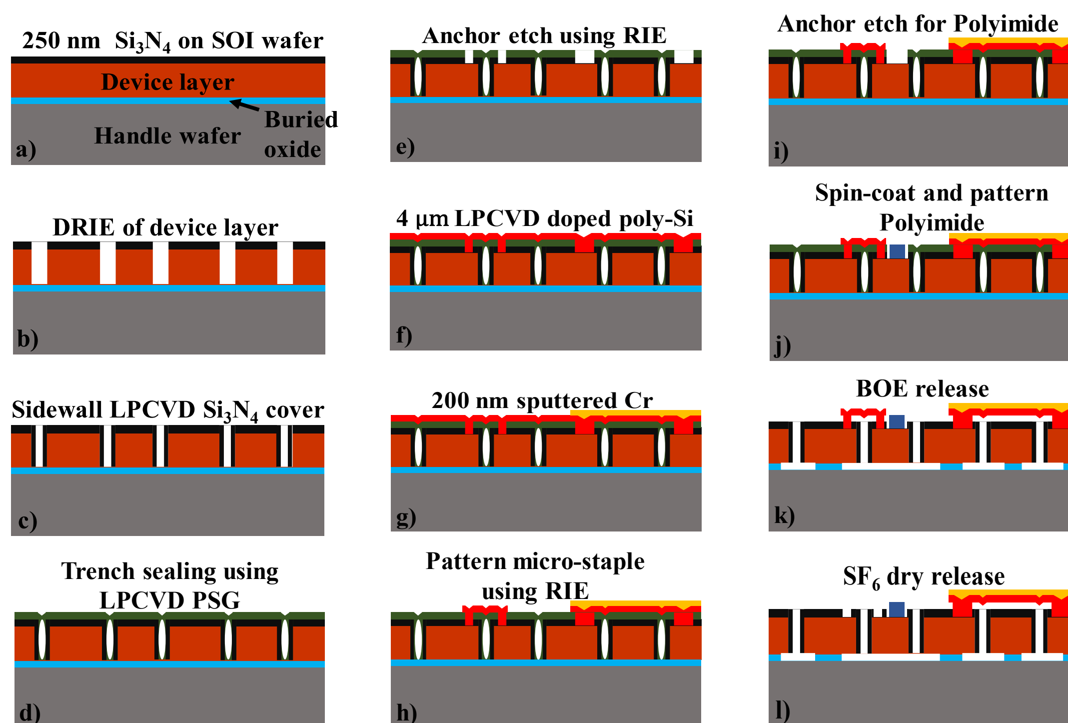

Figure 4: Simplified fabrication procedure of the device.

226 *3.3. Imaging*

227 High-resolution Scanning Electron Microscope (SEM) imaging of the device was done on an FEI
228 Quanta 600 SEM at an accelerating voltage of 20.0 kV to verify the fabricated device structure, as
229 shown in Figure 5(a-c). Figure 5a shows the fabricated device array with the poly-Si jumpers acting
230 as the 2nd level of electrical connections shown in the zoomed in image (Figure 5b). Only the central
231 finger is released during a timed BOE wet etch as the flanking electrodes are much wider and
232 therefore, stay anchored. Zoomed-in image of the central finger is visible in Figure 5c showing the
233 asymmetrically patterned polyimide on the movable beam and the anti-stiction micro-staple pins
234 clamping the central finger to the side electrodes after wet release. The fabricated devices were 900
235 µm long, and the suspended beams were 13.3 µm wide. The air-gap measured between the
236 suspended beam and the side electrode was 4.75 µm. The differential pull-in voltage was calculated
237 to be ~29.5V. The fabricated device had 15 unit cells connected in a parallel circuit.

Preprints (www.preprints.org) | NOT PEER-REVIEWED | Posted: 31 July 2019 doi:10.20944/preprints201907.0357.v1

Peer-reviewed version available at Sensors 2019, 19, 3954; doi:10.3390/s19183954

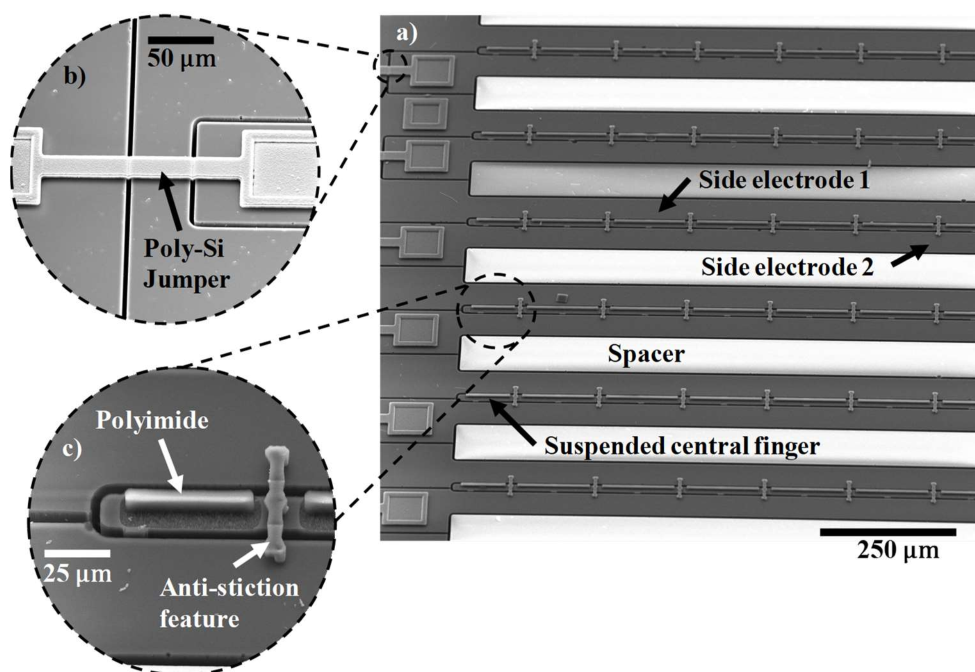

Figure 5: a) LACM sensor array b) Zoomed-in image of a poly-Si jumper over etched trenches acting as the 2nd level of electrical connections c) Magnified view of a suspended central finger with asymmetrically patterned polyimide and anti-stiction micro-staple holder.

238 **4. Testing and Characterization**

239 *4.1. Test Setup*

240 The sensor electrical testing was done at a probe station enclosed in a metallic box to create a
241 localized environment for vapor testing. The enclosing box was grounded to reduce outside
242 interference and noise during measurement. The device capacitance was measured using a Keithley
243 4200A-SCS CVU connected to the probe station at 1MHz frequency using a 30mV AC signal. The
244 noise floor for the test setup was measured to be ~363aF, and the base capacitance of the device was
245 270fF. The chamber was flushed with N_2 gas before testing, and a commercial humidifier placed
246 outside was used to humidify the chamber. The relative humidity (RH) of the chamber was
247 monitored using a commercially available BME-280 [48] chip connected to an Arduino Uno board
248 which reported the chamber humidity to a computer. Dehumidification of the chamber was done by
249 purging the test chamber with N_2 while evacuating the chamber using an in-house vacuum line.

250 *4.2. Sensor action and humidity response*

251 Figure 6a shows the normalized response of the sensor as a function of varying water-vapor
252 concentration at different biasing voltages. Sensor capacitance decreases when operated at no-bias
253 voltage, which we believe, is due to a reduction in overlap area because of undesirable out-of-plane
254 downward deflection of the central cantilever beam when exposed to increasing humidity.
255 Application of a small DC bias voltage results in stiffening of the out of plane spring constant of the
256 central finger due to induced electrostatic levitation as described by Tang et al. [49] which prevents
257 out-of-plane deflection. Figure 6b shows the sensor characteristics at different relative humidity
258 levels as a function of varying bias voltage indicating sensor output amplification as the bias voltage
259 is increased at a constant humidity level. A ~11-fold magnification of sensor response was observed
260 for a bias voltage of 28V compared to when a low bias (5V) voltage was used at 40.83 %RH, as shown
261 in Figure 7. Figure 8 shows the dynamic response of the device when exposed to a relative humidity
262 change from 20-90% and operated at a bias voltage of 28V. Highly repeatable device performance

Preprints (www.preprints.org) | NOT PEER-REVIEWED | Posted: 31 July 2019 doi:10.20944/preprints201907.0357.v1

Peer-reviewed version available at Sensors 2019, 19, 3954; doi:10.3390/s19183954

263 was observed, and no sensor saturation was seen, as shown in Figure 8a. Figure 8b shows the
264 continuous operation of the sensor over five cycles of humidification/dehumidification and shows
265 near zero baseline drift.

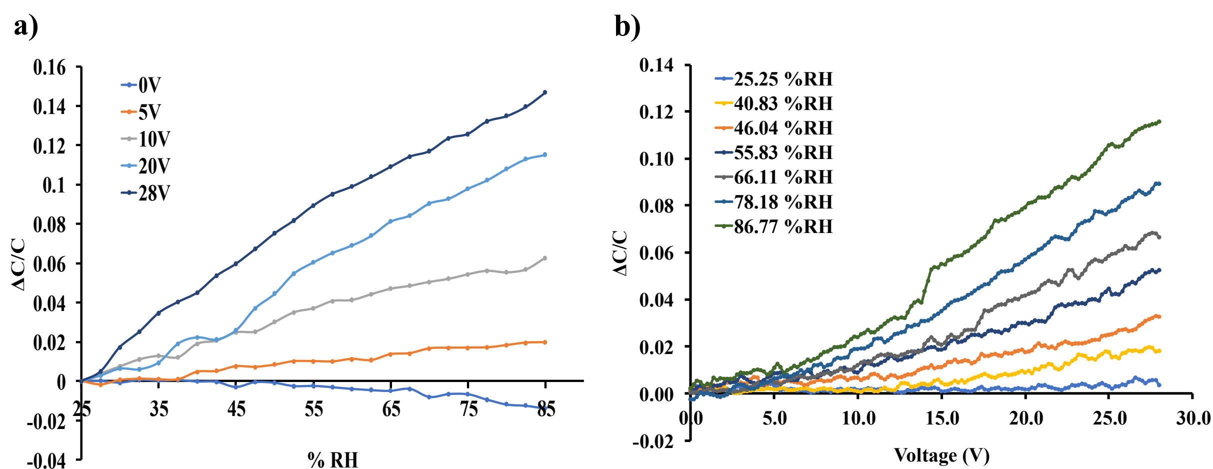

Figure 6: a) Sensor response to varying %RH levels at different DC bias voltage b) Sensor response to a varying bias voltage at different %RH levels.

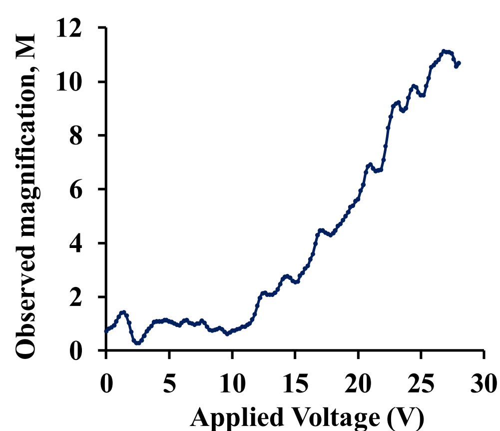

Figure 7: Observed sensor output magnification as a function of applied bias voltage at constant relative humidity.

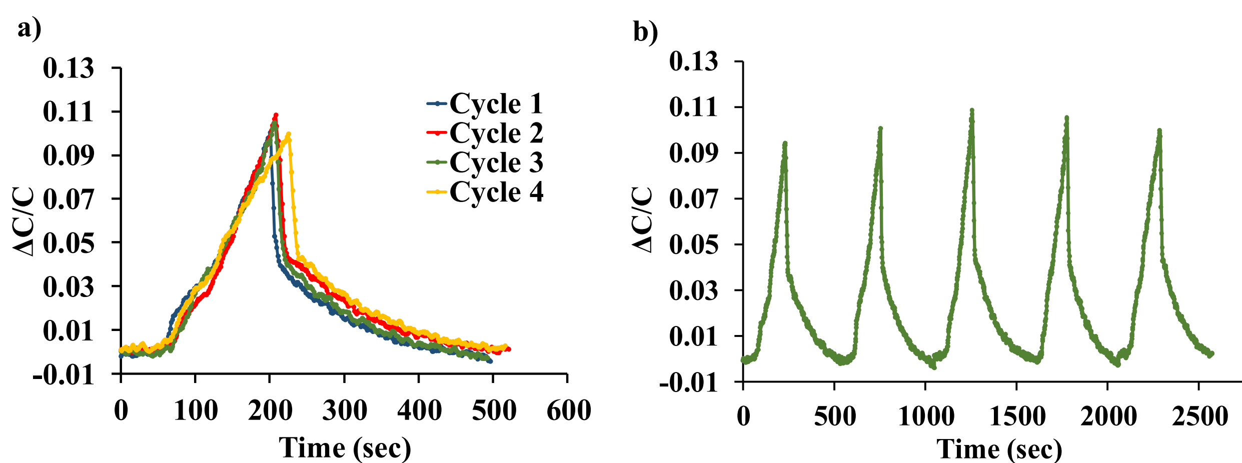

Figure 8: a) Repeatability of LACM sensor tested over four cycles. b) Sensor output over five consecutive cycles of exposure and removal of humidity.

Preprints (www.preprints.org) | NOT PEER-REVIEWED | Posted: 31 July 2019 doi:10.20944/preprints201907.0357.v1

Peer-reviewed version available at Sensors 2019, 19, 3954; doi:10.3390/s19183954

266 *4.3. Model Fitting*

267 Fig 9a shows the equivalent electrical circuit of the LACM sensor. The humidity response of the
268 device was curve-fitted to equation (13), and the plot is shown in Figure 9b. Parameter extraction
269 revealed the mean value of β_p ~ 0.114 $mN.m^{-1}$ per ppm of water vapor and the value of fitting
270 parameters A_o and B_o ranged from 2.5 to 12 and -0.06 to -0.01, respectively. The root-mean-square
271 error was found to be 0.1%, 0.39% and, 0.52% for applied bias voltages 5V, 20V and 28V, respectively.

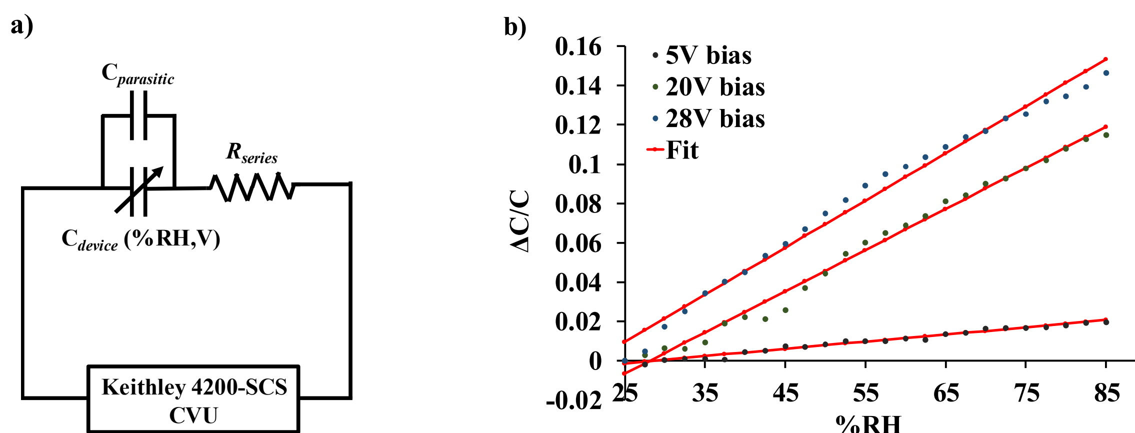

Figure 9: a) Equivalent electrical representation of the LACM sensor b) Normalized change in capacitance of the sensor curve fitted to equation (13).

272 *4.4. Absorption-Desorption Kinetics*

273 The dynamic response of the device is dependent on the moisture absorption induced swelling
274 of the polyimide on the central cantilever beam. This type of behavior can be explained by a modified
275 version of Fick's second law of diffusion. The performance of the LACM sensor can be effectively
276 modeled as described by Sikame Tagne [50]. The desorption kinetics of the sensor is considered as a
277 gradual desorption of water molecules back into the atmosphere and modeled using the Polanyi-
278 Wigner equation [51]. The curve fitted normalized change in capacitance is shown in Figure 10a.
279 Additionally, Figure 10b compares the normalized device response to that of a commercially
280 available BME-280 [48] reference sensor chip. It can be observed from the plot that the LACM sensor
281 closely follows the response of the reference chip which has a response time of 1s [48] with both the
282 sensors reaching their maximum output at the same time.

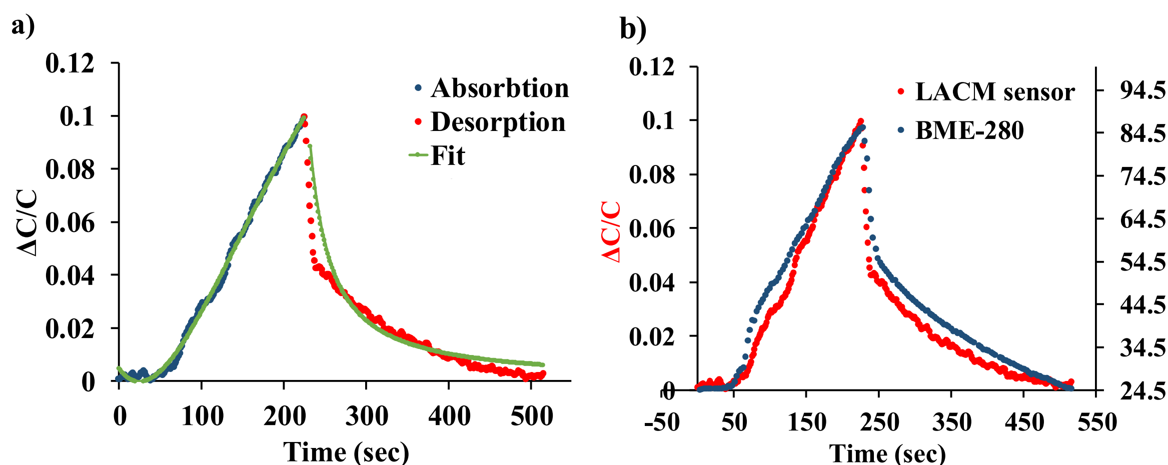

Figure 10: a) Dynamic response of the LACM sensor curve fitted to Fick's second law and the Polanyi-Wigner equation. b) Comparison of the LACM sensor performance to a commercially available BME-280 reference chip

Preprints (www.preprints.org) | NOT PEER-REVIEWED | Posted: 31 July 2019 doi:10.20944/preprints201907.0357.v1

Peer-reviewed version available at Sensors 2019, 19, 3954; doi:10.3390/s19183954

5. Conclusions

We presented the design, fabrication, and response of a batch-fabricated capacitive polymer-based humidity sensor based on mechanical leveraging and parametric amplification. The device exploits the electrostatic lateral instability of MEMS structures to achieve a noiseless intrinsic gain, which helps in achieving a better SNR. A ~11-fold magnification in sensor output was achieved by applying a 28V DC bias voltage to the device at constant water vapor concentration due to spring softening. We demonstrate an unassisted and completely recoverable change of 11% in capacitance value when subjected to a humidity change from 25-85%. The dynamic response of the sensor was also characterized, and the sensor showed a comparable response to a commercially available reference chip with ~1s response time. A mathematical model to accurately describe the sensor action and sensor dynamics has also been presented. Such a sensor is an excellent candidate for low-power, low-cost, and sensitive vapor-sensor for applications in IoT based frameworks.

Author Contributions: R.L. designed, fabricated and tested all devices as well as performed characterization of the LACM sensor, wrote and proofread the manuscript. research articles. A.B. assisted in the device testing, mathematical modeling, manuscript preparation and proofreading. A.M. and M.K. assisted in manuscript proofreading. H.K. helped in the experimental setup. C.H.M. helped in concept inception, device testing, fabrication, and analysis of results as well as the preparation and proofreading of the manuscript.

Funding: This research received no external funding.

Acknowledgments: The authors would like to thank the staff at the University of Utah Nanofab and, the Surface Analysis Lab for their assistance in fabricating and imaging the LACM sensor.

Conflicts of Interest: The authors declare no conflict of interest the results.

References

1. N. Yamazoe, Y. Shimizu, Humidity sensors: Principles and applications, Sensors and Actuators. 10 (1986) 379–398. doi:https://doi.org/10.1016/0250-6874(86)80055-5.
2. Z. Chen, C. Lu, Humidity Sensors: A Review of Materials and Mechanisms, Sens. Lett. (2005). doi:10.1166/sl.2005.045.
3. Z.M.M. Rittersma, Recent achievements in miniaturised humidity sensors - A review of transduction techniques, Sensors Actuators, A Phys. 96 (2002) 196–210. doi:10.1016/S0924-4247(01)00788-9.
4. C. Bariáin, I.R. Matías, F.J. Arregui, M. López-Amo, Optical fiber humidity sensor based on a tapered fiber coated with agarose gel, Sensors Actuators, B Chem. (2000). doi:10.1016/S0925-4005(00)00524-4.
5. M. Penza, G. Cassano, Relative humidity sensing by PVA-coated dual resonator SAW oscillator, Sensors Actuators, B Chem. (2000). doi:10.1016/S0925-4005(00)00448-2.
6. A. Banerjee, R. Likhite, H. Kim, C.H. Mastrangelo, Quantum Tunneling Hygrometer with Temperature Stabilized Nanometer Gap, (2019). http://arxiv.org/abs/1906.02451 (accessed June 7, 2019).
7. R. Fenner, E. Zdankiewicz, Micromachined Water Vapor Sensors: A Review of Sensing Technologies, IEEE Sens. J. (2001). doi:10.1109/7361.983470.
8. Why control humidity in a cleanroom? | Solid State Technology, (n.d.). https://electroiq.com/2003/10/why-control-humidity-in-a-cleanroom/ (accessed June 6, 2019).
9. N. Wang, N. Zhang, M. Wang, Wireless sensors in agriculture and food industry - Recent development and future perspective, Comput. Electron. Agric. (2006). doi:10.1016/j.compag.2005.09.003.
10. C.A. Balaras, E. Dascalaki, A. Gaglia, HVAC and indoor thermal conditions in hospital operating rooms, Energy Build. (2007). doi:10.1016/j.enbuild.2006.09.004.
11. J.C. Zhao, J.F. Zhang, Y. Feng, J.X. Guo, The study and application of the IOT technology in agriculture, in: Proc. - 2010 3rd IEEE Int. Conf. Comput. Sci. Inf. Technol. ICCSIT 2010, 2010. doi:10.1109/ICCSIT.2010.5565120.
12. A. Banerjee, T. Ghosh, R. Likhite, N. Hasan, H. Kim, C.H. Mastrangelo, Electrical detection of proteins using batch-fabricated vertical metal nanogap break-junctions, in: 20th Int. Conf. Miniaturized Syst. Chem. Life Sci. MicroTAS 2016, 2016.
13. A. Banerjee, N. Farhoudi, C. Ghosh, C.H. Mastrangelo, H. Kim, S.J. Broadbent, R. Looper, Picowatt gas sensing and resistance switching in tunneling nano-gap electrodes, in: Proc. IEEE Sensors, 2017. doi:10.1109/ICSENS.2016.7808637.

Peer-reviewed version available at Sensors 2019, 19, 3954; doi:10.3390/s19183954

334 14. A. Banerjee, S.-U.H. Khan, S. Broadbent, R. Likhite, R. Looper, H. Kim, C.H. Mastrangelo, Batch-Fabricated
335 α -Si Assisted Nanogap Tunneling Junctions, Nanomaterials. 9 (2019) 727. doi:10.3390/nano9050727.
336 15. E. Traversa, Ceramic sensors for humidity detection: the state-of-the-art and future developments, Sensors
337 Actuators B. Chem. (1995). doi:10.1016/0925-4005(94)01268-M.
338 16. Y. Sakai, Y. Sadaoka, M. Matsuguchi, Humidity sensors based on polymer thin films, Sensors Actuators, B
339 Chem. (1996). doi:10.1016/S0925-4005(96)02019-9.
340 17. S. Chatzandroulis, A. Tserepi, D. Goustouridis, P. Normand, D. Tsoukalas, Fabrication of single crystal Si
341 cantilevers using a dry release process and application in a capacitive-type humidity sensor, Microelectron.
342 Eng. 61–62 (2002) 955–961. doi:10.1016/S0167-9317(02)00448-3.
343 18. C.Y. Lee, G.B. Lee, Micromachine-based humidity sensors with integrated temperature sensors for signal
344 drift compensation, J. Micromechanics Microengineering. (2003). doi:10.1088/0960-1317/13/5/313.
345 19. M.J. Thompson, D.A. Horsley, Parametrically amplified MEMS magnetometer, in: TRANSDUCERS 2009 -
346 15th Int. Conf. Solid-State Sensors, Actuators Microsystems, 2009. doi:10.1109/SENSOR.2009.5285917.
347 20. D.R. Baselt, B. Fruhberger, E. Klaassen, S. Cemalovic, C.L. Britton, S. V. Patel, T.E. Mlsna, D. McCorkle, B.
348 Warmack, Design and performance of a microcantilever-based hydrogen sensor, Sensors Actuators, B
349 Chem. (2003). doi:10.1016/S0925-4005(02)00315-5.
350 21. R. Likhite, A. Banerjee, H. Kim, C.H. Mastrangelo, Self-Leveling Micromechanical Gas Sensors, in: Proc.
351 IEEE Sensors, IEEE, 2018: pp. 1–4. doi:10.1109/ICSENS.2018.8589579.
352 22. M. Álvarez, L.G. Carrascosa, M. Moreno, A. Calle, Á. Zaballos, L.M. Lechuga, C. Martínez-A, J. Tamayo,
353 Nanomechanics of the formation of DNA self-assembled monolayers and hybridization on
354 microcantilevers, Langmuir. (2004). doi:10.1021/la0489559.
355 23. K.M. Hansen, T. Thundat, Microcantilever biosensors, Methods. 37 (2005) 57–64.
356 doi:https://doi.org/10.1016/j.ymeth.2005.05.011.
357 24. Y. Yang, H.F. Ji, T. Thundat, Nerve agents detection using a Cu2+/L-cysteine bilayer-coated
358 microcantilever, J. Am. Chem. Soc. (2003). doi:10.1021/ja028181n.
359 25. M. Sharma, E.H. Sarraf, R. Baskaran, E. Cretu, Parametric resonance: Amplification and damping in MEMS
360 gyroscopes, Sensors Actuators A Phys. 177 (2012) 79–86. doi:10.1016/J.SNA.2011.08.009.
361 26. H. Droogendijk, C.M. Bruinink, R.G.P. Sanders, A.M.K. Dagamseh, R.J. Wiegerink, G.J.M. Krijnen,
362 Improving the performance of biomimetic hair-flow sensors by electrostatic spring softening, J.
363 Micromechanics Microengineering. 22 (2012) 065026. doi:10.1088/0960-1317/22/6/065026.
364 27. A. Banerjee, S.S. Pandey, N. Banerjee, N. Hasan, C.H. Mastrangelo, A milli-volt triggered MEMS paddle
365 switch, in: 2015 IEEE SENSORS - Proc., 2015. doi:10.1109/ICSENS.2015.7370441.
366 28. S.S. Pandey, N. Banerjee, A. Banerjee, N. Hasan, H. Kim, C.H. Mastrangelo, High-sensitivity parametrically
367 amplified chemo-mechanical vapor sensors, in: 2015 IEEE SENSORS - Proc., 2015.
368 doi:10.1109/ICSENS.2015.7370582.
369 29. R. Likhite, S.S. Pandey, A. Banerjee, H. Kim, C.H. Mastrangelo, Amplified chemomechanical comb gas
370 sensor, in: Proc. IEEE Sensors, IEEE, 2017: pp. 1–3. doi:10.1109/ICSENS.2016.7808784.
371 30. S. Singamaneni, M.E. McConney, M.C. LeMieux, H. Jiang, J.O. Enlow, T.J. Bunning, R.R. Naik, V. V.
372 Tsukruk, Polymer-silicon flexible structures for fast chemical vapor detection, Adv. Mater. (2007).
373 doi:10.1002/adma.200701419.
374 31. W. Zhang, G. Meng, Nonlinear dynamical system of micro-cantilever under combined parametric and
375 forcing excitations in MEMS, Sensors Actuators A Phys. 119 (2005) 291–299. doi:10.1016/J.SNA.2004.09.025.
376 32. A.M. Elshurafa, K. Khirallah, H.H. Tawfik, A. Emira, A.K.S. Abdel Aziz, S.M. Sedky, Nonlinear dynamics
377 of spring softening and hardening in folded-mems comb drive resonators, J. Microelectromechanical Syst.
378 (2011). doi:10.1109/JMEMS.2011.2148162.
379 33. H. Torun, K.K. Sarangapani, F.L. Degertekin, Spring constant tuning of active atomic force microscope
380 probes using electrostatic spring softening effect, Appl. Phys. Lett. (2007). doi:10.1063/1.2827190.
381 34. S. Krylov, Y. Gerson, T. Nachmias, U. Keren, Excitation of large-amplitude parametric resonance by the
382 mechanical stiffness modulation of a microstructure, J. Micromechanics Microengineering. 20 (2010)
383 015041. doi:10.1088/0960-1317/20/1/015041.
384 35. T.B. Gabrielson, Mechanical-Thermal Noise in Micromachined Acoustic and Vibration Sensors, IEEE Trans.
385 Electron Devices. (1993). doi:10.1109/16.210197.
386 36. A.N. Cleland, M.L. Roukes, Noise processes in nanomechanical resonators, J. Appl. Phys. (2002).
387 doi:10.1063/1.1499745.

Preprints (www.preprints.org) | NOT PEER-REVIEWED | Posted: 31 July 2019 doi:10.20944/preprints201907.0357.v1

Peer-reviewed version available at Sensors 2019, 19, 3954; doi:10.3390/s19183954

388 37. P.R. Gray, Analysis and design of analog integrated circuits, Wiley, 2009. https://www.wiley.com/en-
389 us/Analysis+and+Design+of+Analog+Integrated+Circuits%2C+5th+Edition-p-9780470245996 (accessed
390 June 21, 2019).
391 38. Steve Taranovich, Humidity Sensors and Signal Conditioning Choices | DigiKey, Electron. Prod. (2011).
392 https://www.digikey.com/en/articles/techzone/2011/oct/humidity-sensors-and-signal-conditioning-
393 choices (accessed June 20, 2019).
394 39. Ville Kaajakari, Noise in micromechanical systems, (n.d.).
395 http://www.kaajakari.net/~ville/research/tutorials/tutorials.shtml (accessed June 19, 2019).
396 40. R. Buchhold, A Study on the Microphysical Mechanisms of Adsorption in Polyimide Layers for
397 Microelectronic Applications, J. Electrochem. Soc. (2006). doi:10.1149/1.1838906.
398 41. M. Godin, V. Tabard-Cossa, P. Grütter, P. Williams, Quantitative surface stress measurements using a
399 microcantilever, Appl. Phys. Lett. 79 (2001) 551–553. doi:10.1063/1.1387262.
400 42. N. Banerjee, A. Banerjee, N. Hasan, S.S. Pandey, B.P. Gogoi, C.H. Mastrangelo, A Monolithically Integrated
401 Multisensor Platform, IEEE Sens. J. (2016). doi:10.1109/JSEN.2016.2593698.
402 43. N. Banerjee, A. Banerjee, S.S. Pandey, B.P. Gogoi, C.H. Mastrangelo, Encroachment and line of sight
403 blocking in micro-cavity sealing, in: 2015 IEEE SENSORS - Proc., 2015. doi:10.1109/ICSENS.2015.7370691.
404 44. HD Microsystems, HD – 4100 SERIES Photodefineable Polyimide, (n.d.).
405 http://www.hdmicrosystems.com/ec/liquid-polyimides-and-pbo-precursors/products/sub-products/hd-
406 4100-series.html (accessed June 2, 2019).
407 45. C.H. Mastrangelo, Suppression of Stiction in MEMS, MRS Proc. (1999). doi:10.1557/proc-605-105.
408 46. R. Maboudian, W.R. Ashurst, C. Carraro, Self-assembled monolayers as anti-stiction coatings for MEMS:
409 Characteristics and recent developments, Sensors Actuators, A Phys. (2000). doi:10.1016/S0924-
410 4247(99)00337-4.
411 47. A. Banerjee, S.S. Pandey, C.H. Mastrangelo, MEMS stiction supression with sacrificial polystyrene
412 nanoparticles, in: Proc. IEEE Sensors, 2017. doi:10.1109/ICSENS.2017.8233922.
413 48. Bosch Sensortec, BME280 - Combined humidity, pressure and temperature sensor, Datasheet. (2015).
414 https://www.bosch-sensortec.com/en/bst/products/all_products/bme280 (accessed May 29, 2019).
415 49. W.C. Tang, M.G. Lim, R.T. Howe, Electrostatic Comb Drive Levitation and Control Method, J.
416 Microelectromechanical Syst. (1992). doi:10.1109/JMEMS.1992.752508.
417 50. N.R. Sikame Tagne, E. Njeugna, M. Fogue, J.-Y. Drean, A. Nzeukou, D. Fokwa, Study of Water Absorption
418 in Raffia vinifera Fibres from Bandjoun, Cameroon , Sci. World J. (2014). doi:10.1155/2014/912380.
419 51. R. Luna, C. Millán, M. Domingo, C. Santonja, M.Á. Satorre, Experimental study of the frequency factor in
420 the Polanyi–Wigner equation: The case of C2H6, Vacuum. 122 (2015) 154–160.
421 doi:https://doi.org/10.1016/j.vacuum.2015.09.021.
422